

Weak Radio Frequency Signal Detection Based on Piezo-Opto-Electro-Mechanical System: Architecture Design and Sensitivity Prediction

Shanchi Wu, Chen Gong, Chengjie Zuo, Shangbin Li, Junyu Zhang, Zhongbin Dai, Kai Yang, Ming Zhao, Rui Ni, Zhengyuan Xu, and Jinkang Zhu

Abstract—We propose a novel radio-frequency (RF) receiving architecture based on micro-electro-mechanical system (MEMS) and optical coherent detection module. The architecture converts the received electrical signal into mechanical vibration through the piezoelectric effect and adopts an optical detection module to detect the mechanical vibration. We analyze the response function of piezoelectric film to an RF signal, the noise limited sensitivity of the optical detection module and the system transfer function in the frequency domain. Finally, simple on-off keying (OOK) modulation with carrier frequency 1 GHz is used to numerically evaluate the detection sensitivity. The result shows that, considering the main noise sources in system, the signal detection sensitivity can reach around -118.9 dBm at bandwidth 5 MHz. Such sensitivity significantly outperforms that of the currently deployed Long Term Evolution (LTE) system.

Index Terms—weak signal, radio frequency communication, sensitivity power level, piezo-opto-electro-mechanical system, piezoelectric film, optical coherent detection.

I. INTRODUCTION

HIGH sensitivity signal detection of weak radio frequency (RF) signals is a long and ubiquitous challenge, crucial in radio astronomy, medical imaging, navigation, and communication [1]. Due to rapid development of wireless communications, more compact amplifier, filter, oscillator and mixer circuits are being designed and delivered. Currently, due to wider usage of higher frequency for wireless communication, the faster signal attenuation also requires high-sensitivity signal detection to extend the communication range. Moreover, the communication system for future Internet of Things embraces lower transmission power to extend the battery life, which requires higher receiver-side detection sensitivity [2]–[7].

On the other hand, the state-of-the-art signal detection operates using the components based on electro-mechanical interaction. The interaction between optics, electronics and mechanics can further increase the detection sensitivity. The main limit of signal detection sensitivity originates from all

types of noise, while the conversion of mechanically mediated microwave and optical signals can theoretically be close to unit efficiency and zero noise temperature [8]–[14]. Applying such systems to the nano-scale systems (limiting electromagnetic and displacement fields to submicron sizes) provides opportunities for enhancing the coupling strength and increase the receiver sensitivity [15].

From the general theory of electromagnetics, the control of the propagation and conversion of light can be achieved by changing the refractive index in a particular medium, or by changing the physical boundary between different media. The refractive index of materials can be changed in a variety of ways, such as electric field [16] and temperature [15]. The disadvantage of these methods lies in the weak variations. In contrast, the change of mechanical displacement has a significant effect on light control (e.g. the phase of the beam and the frequency of the light in cavity), and the movement of the machinery can be easily driven by electrostatic or piezoelectric force. The study of cavity optical mechanics [17], [18] shows that the nano-mechanical resonators can be strongly coupled with microwaves [19]–[21] or optical fields [22], [23]. Such characteristics increase the possibility for us to convert the RF signal to the optical signal. It is reported that high sensitivity nanometer opto-electro-mechanical system can be achieved by using high quality factor nano-film [1]. Through the coupling inductor, the input microwave signal enters the LC circuit and is loaded on the film. Under the electrostatic force, the film vibrates and the laser phase incident on the surface changes. Consequently, the small film vibration can be detected at the back end. However, electrostatically driven nanoscale opto-electro-mechanical system has a low working frequency range (several Mega Hertz), which cannot meet the Giga Hertz frequency in RF communication systems. Therefore, a piezoelectric actuated opto-electro-mechanical system is desirable for RF frequency up to Giga Hertz. Although piezoelectric micro-electro-mechanical system (MEMS) resonators have been effectively used as frequency determining elements [24]–[26], there is no open report on using the vibration characteristics of piezoelectric MEMS for communication applications.

In this work, we propose an RF receiving system architecture based on the piezoelectric MEMS and optical coherent detection, called piezo-opto-electro-mechanical system (POEMS). To evaluate its feasibility in signal detection, we analyze the response function of piezoelectric film to an RF signal, and obtain the surface vibration equation. Based on

This work was supported in part by National Key Research and Development Program of China under (Grant 2018YFB1801904), Key Program of National Natural Science Foundation of China (Grant No. 61631018), Key Research Program of Frontier Sciences of CAS (Grant No. QYZDY-SSW-JSC003), and Huawei Innovation Project.

Shanchi Wu, Chen Gong, Chengjie Zuo, Shangbin Li, Junyu Zhang, Zhongbin Dai, Kai Yang, Ming Zhao, Zhengyuan Xu, and Jinkang Zhu are with University of Science and Technology of China, Email address: {wsc0807, jy970102, dzb123, wulikai}@mail.ustc.edu.cn, {cgong821, czuo, shbli, zhaoming, zuzy, jkzhu}@ustc.edu.cn.

Rui Ni is with Huawei Technology, Email address: raney.nirui@huawei.com.

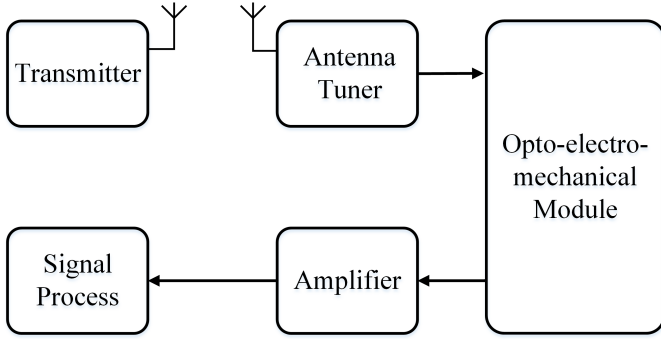


Fig. 1. The diagram of the proposed system.

the noise limited sensitivity of the optical detection module, the detection sensitivity to different frequencies signals is given. Furthermore, we characterize the transfer function of POEMS in the frequency domain, based on the first order perturbation theory. Finally, considering noise signals from wireless channel, coupling circuit, piezoelectric film and optical module, we evaluate the performance of an on-off keying (OOK) modulation from bandwidths 1 kHz to 10 MHz with carrier frequency 1 GHz. It is calculated that the detection sensitivity can be significantly improved, compared with that of the currently used communication system at bandwidths 3.75 kHz and 5 MHz. Such results envisage the promise of using POEMS for high-sensitivity signal detection.

The remainder of this paper is organized as follows. In Section II, we elaborate the proposed system model under consideration. In Section III, we investigate the response functions of each module and the entire system, and provide the noise characterization and sensitivity limit. Numerical results of each module are given in Section IV. In Section V, we perform link simulation of our proposed system and evaluate the system performance. Finally, Section VI provides the concluding remarks.

II. SYSTEM MODEL

A. System Diagram

We consider a novel piezo-opto-electro-mechanical structure for weak power detection. The input signal is converted to mechanical vibration through the piezoelectric film, and the mechanical vibration is then converted to optical signal through an optical measurement system. The physical size of the piezoelectric film is in the order of submillimeter; and the band pass characteristics of piezoelectric film can realize frequency filtering effect. The diagram of the system under consideration is shown in Figure 1.

Piezoelectric film coated with reflective surface acts as an "end mirror" of the optical detection module. When the piezoelectric film deforms, the end mirror position changes. The movement of piezoelectric film, which is driven by the RF signal, can be detected by the optical module output. As shown in Figure 2, the RF signal is coupled into the resonant circuit consisting of inductors and piezoelectric film. The film vibrates under the RF signal excitation, and the detected signal of the photodetector varies accordingly. The piezoelectric film and

optical module will be characterized in detail in the subsequent subsections.

Such design can achieve high sensitivity by combining piezoelectric MEMS with the optical detection module. Due to the fundamental dynamic theory, electrostatic driven film oscillators cannot work at high frequencies, e.g., Giga Hertz. Piezoelectric actuated thin film oscillators can be adopted to solve such issue, such that high frequency signals can be detected with high sensitivity.

B. Piezoelectric Film

Piezoelectric materials have the property that an electric field applied in the direction of polarization can lead to the deform, due to the polarization effect of the dielectric. Aluminium nitride (AlN) is one of them, which has high thermal conductivity at low temperatures, good mechanical strength, high resistivity and corrosion resistance, and high resonant frequency. Thus, AlN resonators are attractive building blocks for electromechanical devices in micrometer and nanometer scales [27]–[29].

The piezoelectric body can generate certain vibration mode activated by the external electric field. If an electric field is applied along a certain direction of the piezoelectric body, the non-zero piezoelectric constant associated with that direction can be employed to determine which vibration mode is likely to be excited. For weak RF signal reception, the thin film system has a linear response to external field strength. Although its three-dimensional system displacement is difficult to characterize, we adopt one directional responses for real applications, which approximately follows Hook law.

As shown in Figure 3 (a), the piezoelectric film adopted exhibits a sandwich structure, with an AlN thin film coated with metal layer as electrodes on the top and bottom surfaces, with length L , width W and thickness L_T . Figure 3 (b) illustrates the shape in cross section, with and without electrical signal. In order to achieve vibration in the thickness direction and ignore the effects of vibration in other directions, the length and width of the film should be much larger than its thickness, i.e., $L, W \gg L_T$. It is important to note that the resonance frequency of the film (vibration in the direction of thickness) under consideration is determined by the thickness. Given piezoelectric material, the resonance frequency f_0 is inversely proportional to thickness. When a signal of certain amplitude with frequency f is applied between two electrodes, the maximum deformation occurs at $f = f_0$.

C. Optical Module

Laser interferometer, as a type of precise optical measuring instrument based on the light interference, can measure the difference of optical paths generated by other certain relevant physical quantities. A typical laser interferometer consists of laser light source, splitting mirror, reflection mirror, polarizing optics and photoelectric detectors. Its basic structure is Michelson interferometer. Any change of optical path difference between two coherent beams will lead to the change of interference field (such as the movement of fringes, etc.), and the optical path change of a coherent beam is

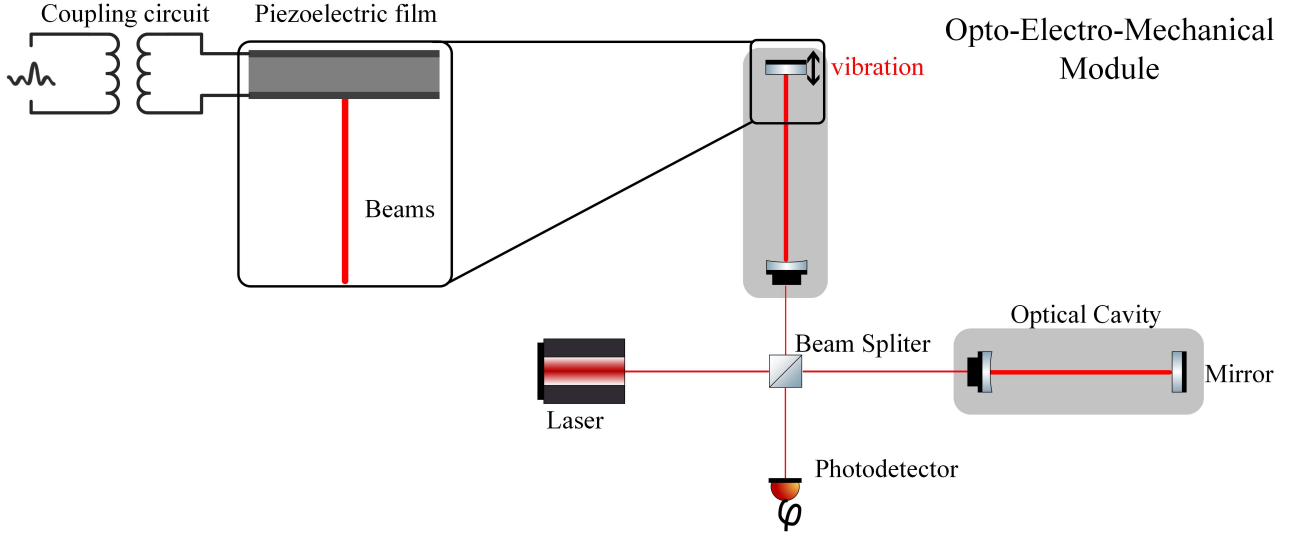


Fig. 2. Diagram of the piezo-opto-electro-mechanical system.

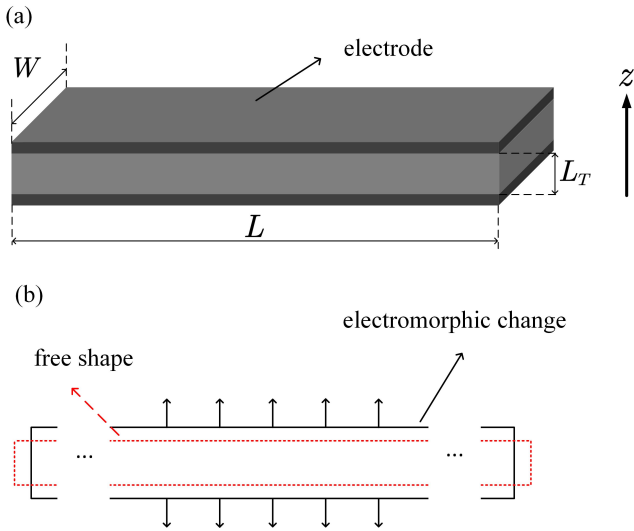


Fig. 3. The sandwich structure of piezoelectric film adopted, with length L , width W and thickness L_T , along with the schematic diagram.

caused by the change of geometric path or refractive index of the medium through which it passes. The modern laser interferometer is based on the frequency stabilized laser with high stability of wavelength, whose measurement accuracy is significantly higher than that of other measurement methods. Optical interferometer has been adopted for measurement in astronomy, optics, engineering surveying, oceanography, seismology, spectrum analysis, quantum physics experiment, remote sensing and radar. The prototype of Laser Interferometer Gravitational-Wave Observatory (LIGO) system is a Michelson optical interferometer [30].

We design the optical module to realize an optical interferometer, which utilizes the superposition of optical wave to obtain the phase information. As the vibration amplitude of

piezoelectric film is tiny under the weak RF signal stimulation, high-precision displacement measurement is required, based on the optical coherent detection following the idea of Michelson interferometer. When a small shift of the end mirror occurs, the signal strength of the photodetector changes accordingly, caused by the phase change of the light in optical arm. In order to achieve higher precision, larger laser power and a longer light arm is desirable. In order to decrease the receiver module size, optical cavity is adopted, which significantly increases the measurement precision [31].

III. SENSITIVITY ANALYSIS

We analyze the response of the piezoelectric film and the optical measurement module, based on which the system transfer function in the frequency domain can be obtained. As a major system degradation factor, the noise components from film, circuits and optical module are characterized. Combined with the transfer function, the sensitivity of the receiver modules can be obtained. The analysis will follow the blocks as shown in Figure 4. Firstly, we give the response of piezoelectric film to signals, which converts electrical signal to mechanical displacement. Secondly, we investigate the response of optical module to mechanical vibration, which converts mechanical signal to optical phase. Then, based on the discrete modules, we can obtain the system transfer function from electrical signal to optical phase. Finally, considering the noise source, the noise limited sensitivity is analyzed.

A. Response of Piezoelectric Film to Signals

The alternating voltage is applied to the piezoelectric vibrator, and the mechanical vibration of the piezoelectric vibrator will be excited by the inverse piezoelectric effect coupling, which will generate strain in the vibrator. Moreover, the mechanical vibration of the vibrator will generate current through the positive piezoelectric effect and feedback back

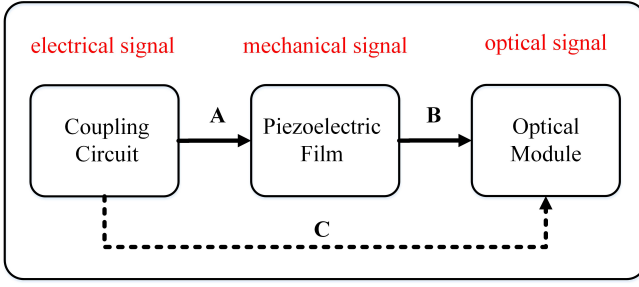


Fig. 4. Diagram of the sensitivity analysis flow.

to the circuit. When the applied driving voltage frequency is close to the eigen mechanical resonance frequency of the oscillator, the resonance will lead to large mechanical vibration amplitude. The overlap of the driving current and the feedback current may increase the current flowing through the oscillator. The impedance and admittance frequency characteristics of piezoelectric vibrators close to resonant frequencies can be approximated by an equivalent circuit.

Assume that the film length and width is significantly larger than the thickness, i.e., $L, W \gg L_T$. The thickness direction is the main factor. Thus, only the effect of stress component T_z is considered, and other stress components can be ignored. As the electrode surface is perpendicular to the z axis, only the effect of electric field component E_z is considered, and other electric field components can also be ignored. In addition, because only the edges of the film are fixed, the central part is free, i.e., the boundary condition of two surfaces in z -axis is free. The stress component T_z is equal to zero, and the electrode surface is equipotential. In this case, we can choose T_z and E_z as independent variables and use the first class of piezoelectric equations as follows,

$$\begin{aligned} T_z &= c^E S_z - e_{33} E_z, \\ D_z &= e_{33} S_z + \epsilon^S E_z, \end{aligned} \quad (1)$$

where T_z, S_z, E_z and D_z represent stress field, strain field, electric field and electric displacement vector components along the z -axis, respectively; c^E is the elastic modulus at constant electric field strength; ϵ^S is the relative permittivity at constant strain field strength; and e_{33} is piezoelectric constant decided by material [32]. Typically, c^E and ϵ^S are treated as constants. Here, all vector variables are expressed as scalars since we only consider one-dimensional vibration. For convenience, in the following derivations, the letter subscript indicating the z direction is neglected, shown as follows,

$$\begin{aligned} T &= c^E S - e_{33} E, \\ D &= e_{33} S + \epsilon^S E. \end{aligned} \quad (2)$$

Letting u represent the particle displacement in z -axis, given that the displacement of the piezoelectric film is treated as an elastic harmonic oscillator, we have

$$\begin{aligned} \frac{\partial^2 u}{\partial t^2} &= \frac{c^D}{\rho} \frac{\partial^2 u}{\partial z^2}, \\ c^D &= c^E + \frac{e_{33}^2}{\epsilon^S}, \end{aligned} \quad (3)$$

where ρ is the mass density of the film and c^D is the elastic modulus at constant electric displacement vector [33].

Considering the separation of variables, i.e., $u(z, t) = Z(z) \cdot e^{j\omega t}$, and defining phase velocity $v_a \triangleq \sqrt{\frac{c^D}{\rho}}$ of the vibration module along the z -axis, the wave equation $Z(z)$ is given as follows,

$$\begin{aligned} \omega^2 Z + \frac{c^D}{\rho} \frac{d^2 Z}{dz^2} &= 0, \\ \frac{d^2 Z}{dz^2} + \frac{\omega^2}{v_a^2} Z &= 0. \end{aligned} \quad (4)$$

Theorem 1 Under excitation signal $V = V_0 \cdot e^{j\omega_r t}$ and free boundary condition $T_{z=0} = T_{z=L_T} = 0$, the surface vibration at $z = L_T$ is given by

$$u(L_T, t) = \frac{e_{33} D_0}{\epsilon^S c^D \beta} \tan\left(\frac{\beta L_T}{2}\right) \cdot e^{j\omega_r t}, \quad (5)$$

where D_0 is the amplitude of electric displacements vector; $\beta \triangleq \frac{\omega_r}{v_a}$ is a defined coefficient; and ω_r is the resonant frequency.

Proof: Please refer to Appendix B-A. ■

In a real system, the relationship between force and strain may not be linear. Accordingly, parameters such as damping coefficient η are introduced to characterize the new system, which can be written as $T = c^D S + \eta \frac{dS}{dt}$.

Under the condition that the displacement of the piezoelectric film is treated as a damped elastic harmonic oscillator, the wave equation satisfied by the displacement in damping system is given by

$$c^D \frac{\partial^2 v}{\partial z^2} + \eta \frac{\partial^3 v}{\partial t \partial z^2} = \rho \frac{\partial^2 v}{\partial t^2}, \quad (6)$$

where $v(z, t) = \partial u(z, t) / \partial t$ represents the particle velocity; ρ represents the mass density of the film [33].

Theorem 2 For piezoelectric film system with damping coefficient η , under the excitation signal $V = V_0 \cdot e^{j\omega_s t}$ and boundary condition $T_{z=0} = T_{z=L_T} = 0$, the surface vibration at $z = L_T$ is given by

$$u(L_T, t) \approx -j \frac{4QV_0 e_{33}}{\pi^2 c^D} \cdot e^{j\omega_s t}, \quad (7)$$

where e_{33} is the piezoelectric constant and $Q = c^D / \eta \omega_s$ is the quality factor; and ω_s is the series resonance frequency.

Proof: Please refer to Appendix B-B. ■

B. Response of Optical Module to Piezoelectric Film Vibration

For classical Michelson interferometer, the beam propagation can be represented by electric field, as shown in Figure 5 [31]. Assuming that all parameters of the optical components are known, the output of optical field is characterized as follows,

$$\begin{aligned} \mathbf{E}_{\text{out}} &= \mathbf{E}_5 + \mathbf{E}_6 \\ &= \mathbf{E}_0 r t \left(e^{i(\varphi_t + \varphi_{r1} + \Phi_1)} + e^{i(\varphi_t + \varphi_{r2} + \Phi_2)} \right), \end{aligned} \quad (8)$$

where $\varphi_{r1}, \varphi_{r2}$ and φ_t are phase differences caused by reflection of upper surface, lower surface and transmission

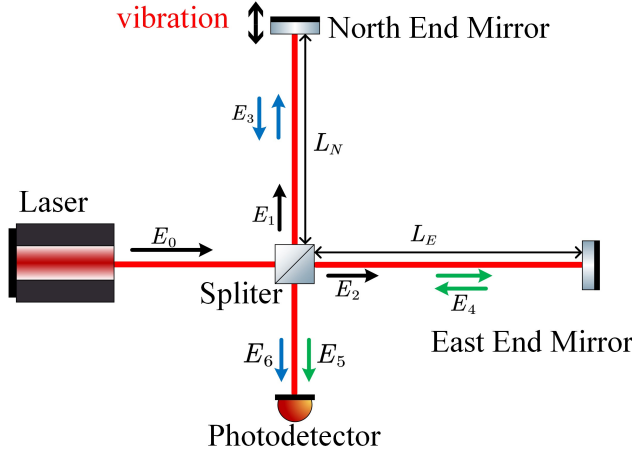


Fig. 5. Diagram of Michelson interferometer.

of the mirror, respectively; r and t are the reflectivity and transmittivity of end mirrors, respectively; Φ_1 and Φ_2 are phase differences caused by optical path differences in arms, respectively; and $R = r^2$ and $T = t^2$.

In a real system, we can only perform direct detection on the optical power or intensity. It is difficult to obtain the optical signal frequency of the commonly used laser directly through the photoelectric sensor. A common solution is to detect the beat of the coherent signal, which is the envelope of the intensity of two overlapping and coherent fields. For the output light field with two frequency components $\mathbf{E} = E_0 [\cos(\omega_1 t) + \cos(\omega_2 t)]$, the corresponding output power is

$$P = E_0^2 \left(\cos^2(\omega_1 t) + \cos^2(\omega_2 t) + \cos(\omega_+ t) + \cos(\omega_- t) \right), \quad (9)$$

where $\omega_+ = \omega_1 + \omega_2$ and $\omega_- = \omega_1 - \omega_2$.

For any interferometer systems, the optical arm length variation will affect the laser propagation in space and cause the phase variation. In order to analyze the influence of the moving end mirror amplitude and frequency on the output sideband signal, we apply periodic modulation signal $x_m = a_s \cos(\omega_s t + \varphi_s)$ to the optical arm, as shown in Figure 5. We have the following results on the output signal of the light field. The output signal of the light field after the reflection signals from the N-end mirror and E-end mirror, combined by the beam splitting mirror, is given by

$$\begin{aligned} \mathbf{E}_{\text{out}} &= \mathbf{E}_0 r t \left(e^{i(\varphi_l + \varphi_{r1} + \Phi_1 + 2k_0 x_m)} + e^{i(\varphi_l + \varphi_{r2} + \Phi_2)} \right) \\ &= \mathbf{E}_0 r t \left(e^{i(\varphi_l + \varphi_{r1} + \Phi_1)} (1 + k_0 a_s (s^+ + s^-)) \right. \\ &\quad \left. + e^{i(\varphi_l + \varphi_{r2} + \Phi_2)} \right), \end{aligned} \quad (10)$$

where E_0 , k_0 and ΔL are the amplitude, wave vector and optical arm length differences of the carrier field, respectively; $s^+ = e^{i(\omega_s t + \varphi_s + \pi/2)}$ and $s^- = e^{-i(\omega_s t + \varphi_s - \pi/2)}$ are upper and lower signal sidebands, respectively [31].

Theorem 3 Assuming that the injection light power is P_0 and photoelectric responsivity of the photodetector is $\alpha(A/W)$, the

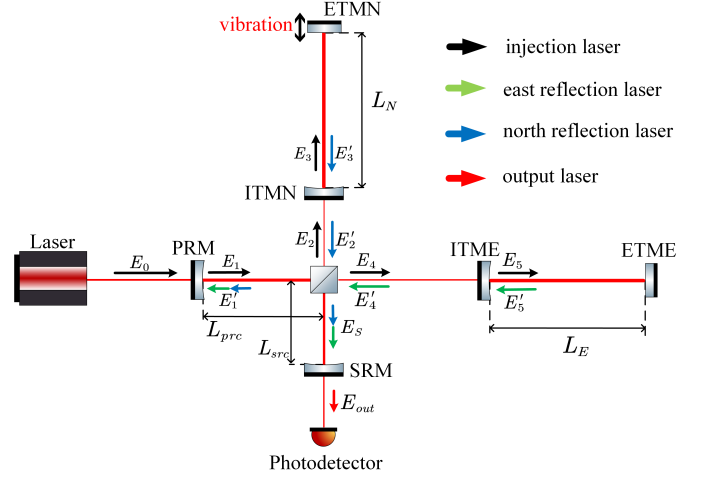


Fig. 6. Diagram of dual-recycled Fabry-Perot-Michelson interferometer.

output current of the Michelson interferometer is given by

$$I_{\text{out}} = \alpha P_0 \left[\cos^2(k_0 \Delta L) + k_0 a_s \sin(2k_0 \Delta L) \cos(\omega_s t + \varphi_s) \right]. \quad (11)$$

Proof: Please refer to Appendix B-C. ■

We can utilise one mirror in front of splitter and photodetector to increase the light power inside the interferometer and obtain higher sensitivity [31]. As shown in Figure 6, the mirror PRM and splitter form a power cycle cavity and the mirror SRM and splitter form a signal cycle cavity. This configuration is most commonly called dual-recycled Fabry-Perot-Michelson interferometer. The arrows show the propagation of light fields, from the injection laser to east mirror reflection laser, north mirror reflection laser and output laser sequentially.

Theorem 4 Assuming that the injection light power is P_0 and photoelectric responsivity of the photodetector is $\alpha(A/W)$, the output current of the dual-recycled Fabry-Perot-Michelson interferometer shown in Figure 6 is given by

$$\begin{aligned} I_{\text{out}} &= \frac{\alpha}{2} G_{\text{PRM}}^2 G_{\text{SRM}}^2 P_0 \left(\left(1 - \frac{t_3^2 e^{-i2k_0 L_E}}{1 - e^{-i2k_0 L_E}} \right) \right. \\ &\quad \left. + \left(1 - \frac{t_1^2 e^{-i2k_0 L_N}}{e^{-i2k_0 x_m} - e^{-i2k_0 L_N}} \right) \right)^2, \end{aligned} \quad (12)$$

where G_{PRM} and G_{SRM} are light power gain and signal power gain of power cycling cavity and signal cycling cavity, respectively; t_1 , t_3 are transmission coefficient of mirror ITMN and ITME, respectively.

Proof: Please refer to Appendix B-D. ■

C. Transfer Function of Piezo-Opto-Electro-Mechanical System in the Frequency Domain

In general, the internal energy of a piezomechanical system is given by

$$U_{pe} = \frac{1}{2} \int dv \left(\mathbf{T} \cdot \mathbf{d}^T \cdot \mathbf{E} + \mathbf{E} \cdot \mathbf{d} \cdot \mathbf{T} \right), \quad (13)$$

where \mathbf{T} and \mathbf{S} are the stress and strain fields, respectively; and \mathbf{E} and \mathbf{D} are the electric field and electric displacement vector, respectively [34].

For one-dimension condition, the total energy of piezoelectric oscillator is given by

$$\begin{aligned} U &= \frac{1}{2} \int dv [T_z \cdot (s_{33}T_z + d_{33}E_z) + E_z \cdot (d_{33}T_z + \varepsilon_{33}E_z)] \\ &= \frac{1}{2} \int dv (s_{33}T_z^2) + \frac{1}{2} \int dv (\varepsilon_{33}E_z^2) + \\ &\quad \frac{1}{2} \int dv (T_z \cdot d_{33}E_z + E_z \cdot d_{33}T_z) \\ &\triangleq U_p + U_e + U_{pe}, \end{aligned} \quad (14)$$

where U_p , U_e and U_{pe} represent mechanical energy, electrical energy and electromechanical coupling energy, respectively. According to the three parts of energy, the Hamiltonian form is given by,

$$\begin{aligned} H &= \frac{p^2}{2m} + \frac{m\omega_M^2 x^2}{2} + \frac{\phi^2}{2L_0} + \frac{q^2}{2C(x)} + \\ &\quad 2g\sqrt{\frac{m\omega_M}{C(x)\omega_{LC}}}xq - qV, \end{aligned} \quad (15)$$

where x and p are the displacement and momentum, respectively; q and ϕ are the charge and flux, respectively; and g is the electromechanical coupling strength [34]. We have the following results on the transfer function of the proposed piezo-opto-electro-mechanical system.

Theorem 5 Assuming that S_{VV}^{input} , S_{xx} are signal power densities of electric signal and displacement signal of film, respectively, the transfer function of the proposed piezo-opto-electro-mechanical system in the frequency domain is given by

$$T(\omega) = \frac{S_{xx}(\omega)}{S_{VV}^{input}(\omega)} = |G\chi_m^{eff}(\omega)\chi_{LC}(\omega)|^2. \quad (16)$$

where G , χ_m^{eff} and χ_{LC} are coupling coefficient, effective film susceptibility and circuit's susceptibility, respectively.

Proof: Please refer to Appendix B-E. ■

Considering the noises from circuit, film and optical module, the output signal of POEMS is obtained as follows,

$$S_{\varphi\varphi}^{output} = (2k)^2 \left(|G\chi_m^{eff}\chi_{LC}|^2 S_{VV}^{input} + S_{xx}^{th} \right) + S_{\varphi\varphi}^{imp}, \quad (17)$$

where S_{VV}^{input} , S_{xx}^{th} and $S_{\varphi\varphi}^{imp}$ are the power spectral densities of input signal, film harmonic noise and optical phase noise, respectively [1].

D. Noise Characterization

The main noise sources are from circuits, thermal environment and optical module. Firstly, we analyze the electrical noise of the resonant circuit and the dynamic displacement disturbance of film. Secondly, when the classical noise in the system is small enough, the influence of quantum fluctuation noise of the optical module becomes critical. Here we consider two types of noise sources: optical radiation pressure and

quantum fluctuation of light. Finally, combined with the transfer function, the equivalent input noise in electrical domain can be obtained.

1) *Electrical Input Noise:* For LC resonant circuit, inductor thermal noise, shot noise and pink noise are three main types of noises. At low frequencies, the pink noise is several times larger than the shot noise, but our system works in a high frequency and can effectively reduce the influence of pink noise. Besides, since the shot noise is weaker than thermal noise under consideration, we only consider thermal noise. Additional noise due to nonstationary radio frequency interference from cellular phones, vehicles, etc., needs to be considered, but in this analysis, we will concentrate on natural sources only. The total input noise power spectral density can be given by

$$N_{VV}^{electro}(\omega) = 2k_B R_L T, \quad (18)$$

where T is the environment temperature; R_L is the inductor equivalent resistance and k_B is the Boltzmann constant.

2) *Film Thermal Noise:* In the LC resonant circuit, the piezoelectric film acts as a capacitor, whose noise is considered in film thermal noise. Such noise is not white in the frequency domain, while the disturbing force from environment is Gaussian white noise instead. We called this dynamic displacement disturbance of film as its thermal noise, which is driven by a disturbing force from environment.

Theorem 6 In equilibrium, the environment exerts a disturbing force η on the damped harmonic oscillator. According to the white noise hypothesis, $\eta(t)$ satisfy $\langle \eta(t) \rangle = 0$ and $\langle \eta(t)\eta(\tau) \rangle = 2\alpha\delta(t-\tau)$. The equivalent harmonic noise power spectrum of the piezoelectric film is given by

$$N_{xx}^{film}(\omega) = 2\alpha_{ex} |\chi_m(\omega)|^2, \quad (19)$$

where $\alpha_{ex} = \alpha m_{eff}^2$ represents the strength of noise.

Proof: Please refer to Appendix B-F. ■

3) *Optical Module Noise:* In the optical cavity, the equivalent dynamic displacement noises of the film, caused by quantum noise and optical radiation pressure noise, are given by

$$N_{xx}^{imp}(\omega) = \frac{\kappa}{16\bar{n}_{cav}G_{opt}^2} \left(1 + 4\frac{\omega^2}{\kappa^2} \right), \quad (20)$$

and

$$N_{xx}^{FF}(\omega) = \bar{n}_{cav} \frac{4\hbar^2 G_{opt}^2}{\kappa} \left(1 + 4\frac{\omega^2}{\kappa^2} \right)^{-1} |\chi_m(\omega)|^2, \quad (21)$$

respectively, where κ and G are cavity decay and coupling coefficient, respectively; and \bar{n}_{cav} is the average number of photons in cavity [18].

The optical module noise under consideration can be given by

$$\begin{aligned} N_{xx}^{optical}(\omega) &= N_{xx}^{imp}(\omega) + N_{xx}^{FF}(\omega) \\ &= \frac{C}{16\bar{n}_{cav}} + \frac{4\hbar^2 \bar{n}_{cav}}{C} |\chi_m(\omega)|^2 \\ &\geq 2\sqrt{\frac{C}{16\bar{n}_{cav}} \cdot \frac{4\hbar^2 \bar{n}_{cav}}{C}} |\chi_m(\omega)|^2 \\ &= \hbar |\chi_m(\omega)|, \end{aligned} \quad (22)$$

where $C \triangleq \kappa \left(1 + 4 \frac{\omega^2}{\kappa^2}\right) / G_{opt}^2$ is a defined coefficient. It should be noted that the noise of optical module is typically represented by the phase uncertainty. Since the optical module is employed to measure the film vibration, the corresponding phase noise is as follows,

$$N_{\varphi\varphi}^{optical}(\omega) = (2k)^2 N_{xx}^{optical}(\omega), \quad (23)$$

where k is the magnitude of the light wave vector.

4) *Output Noise*: Considering the main noise components in the system, the output noise power spectral density at resonance frequency ω_r is given by

$$N_{\varphi\varphi}^{output} = (2k)^2 \left(\left| G \chi_m^{eff} \chi_{LC} \right|^2 N_{VV}^{electro} + N_{xx}^{film} \right) + N_{\varphi\varphi}^{optical}, \quad (24)$$

where χ_{LC} , χ_m^{eff} and G are introduced in Theorem 5.

E. Sensitivity Limit

According to Eq.17 and Eq.24, the system output signal to noise ratio can be given by

$$SNR = \frac{(2k)^2 S_{VV}^{input} \left| G \chi_m^{eff} \chi_{LC} \right|^2}{(2k)^2 \left(\left| G \chi_m^{eff} \chi_{LC} \right|^2 N_{VV}^{electro} + N_{xx}^{film} \right) + N_{\varphi\varphi}^{optical}}. \quad (25)$$

The reference sensitivity power level of evolved universal terrestrial radio access base station is measured under a throughput requirement for a specified reference measurement channel. The modulation method is QPSK and code rate is 1/3 [35], leading to symbol-level SNR about 0 dB. For the proposed system, the minimum signal power spectral density for SNR=0 dB is given by

$$S_{VV}^{min} = \text{Arg} \{ SNR = 0 \text{ dB} \}. \quad (26)$$

Assuming that the signal bandwidth is B and input impedance is R_i , the minimum signal power is given by

$$P_{min} = \frac{S_{VV}^{min} B}{R_i}. \quad (27)$$

IV. NUMERICAL RESULTS ON THE COMPONENTS

A. Piezoelectric Film

COMSOL Multiphysics® is a large-scale advanced numerical simulation software. To simulate all kinds of physical processes, COMSOL Multiphysics® is adopted to realizes highly accurate numerical simulation with high-efficiency computing performance and outstanding multi field bidirectional direct coupling analysis ability. In order to verify the rationality of sensitivity analysis, the admittance curve of the model was simulated and verified by COMSOL Multiphysics® software [36]. We adopt an AlN film that is 500 microns long, 500 microns wide and 5.5 microns high. The sweep frequency range is set to be 0.85 GHz to 1.15 GHz to include the film resonance frequency. In order to save the running time of the program, the peak response location can be estimated through the theoretical calculation to guide the setting of the sweep frequency range. Finally, the admittance curves is shown in

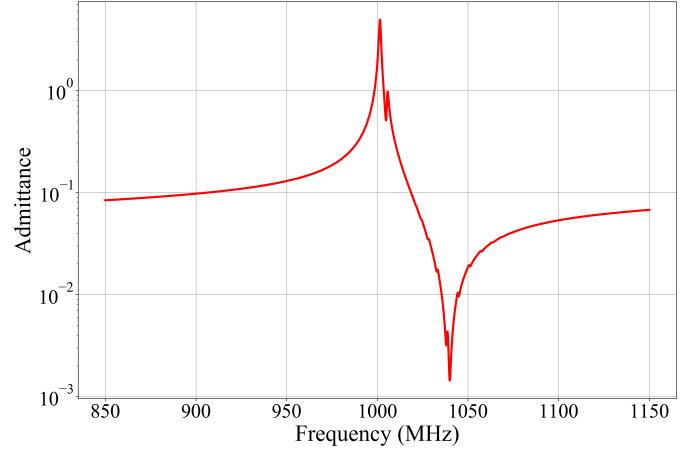


Fig. 7. The simulation of piezoelectric film admittance curves.

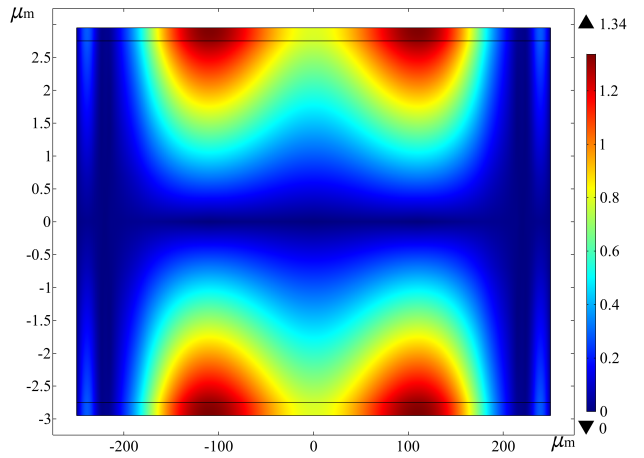


Fig. 8. A regional 2D vibration schematic of piezoelectric film under the RF signal excitation.

Figure 7. The peak response occurs at the position where frequency approximately equals 1001 MHz.

Under the same conditions, the excitation signal frequency is set to be resonance frequency, where the maximum admittance is obtained. Assuming that the amplitude of sinusoidal signal is 1 V with zero offset, the film variation along z-axis is shown in Figure 8. Compared with the vibration equations in Section III-A, the theoretical calculation results can well match the simulation results. The relevant parameters in the simulation can be seen in Table I [37]. According to Eq. 7, the theoretical amplitude of surface displacement is about 1.5 nm. The maximum amplitude shown in Figure 8 is about 1.34 nm, matching the theoretical value within 0.6 dB with the same order of magnitude. The possible reason is the superposition of other vibration modes.

B. Optical Detection Module

Frequency domain INTERferometer SIMulation Software (FINESSE) is a simulation program for interferometers. For a given optical setup, it computes the light field amplitudes at every point in the interferometer assuming a steady state. The interferometer description is translated into a set of

TABLE I
TYPICAL PARAMETERS USED IN COMSOL SIMULATION

Name	Symbol	Value
piezoelectric constant	d_{33}	4.98×10^{-12} C/N
piezoelectric constant	e_{33}	1.55 C/m ²
piezoelectric constant	s_{33}	3.21×10^{-12} m ² /N
modulus of elasticity	c^D	4.19×10^{11} N/m ²
permittivity constant	ϵ^S	7.97×10^{-11} F/m
density of film	ρ	3300 kg/m ³
piezoelectric film thickness	L_T	5.5 μ m
piezoelectric film width	W	500 μ m
piezoelectric film length	L	500 μ m
quality factor of film	Q	1000
resonant frequency of circuit	f_{LC}	1 GHz
resonant frequency of film	f_m	1 GHz

linear equations that are solved numerically, where extensive analysis on the performance prediction be performed, including computing the modulation-demodulation error signals and transfer functions. It can also perform the analysis using plane waves or Hermite-Gauss modes, while the latter one allows computing the effects of mode matching and misalignments. In addition, the error signals for automatic alignment systems can be simulated [38]. We use FINESSE to perform simulation. The parameter settings in the simulation are partly from the reference example [31], while the arm length and components tuning are optimized to obtain peak sensitivity at 1 GHz. Such parameters can provide guidelines for the real fabrication. The simulation includes two parts: response to mirror vibration signal and noise limited sensitivity of optical module. Detailed parameters can be seen in Table II.

1) *Response to Mirror Vibration*: This is a simple FINESSE simulation showing how the response signal can be modulated by the vibration signal on the end mirror. Assume that the north end mirror position in Figure 5 is modulated by a periodic signal $x_m = a_s \cos(\omega_s t + \varphi_s)$, the output light power varies with amplitude a_s and frequency ω_s . In the simulation, the frequencies varies from 0.85 GHz to 1.15 GHz, as shown in Figure 9. Besides, the optical components parameters can significantly change the response characteristics. Specific parameters has been shown in Table II. The maximal gain occurs at the resonant frequency 1 GHz, while the responsivity decreases with the frequency shift. Obviously, the response signal amplitude and power loss coefficient are negatively correlated. We scale the response signal amplitude to photocurrent with unit A/pm. The scaling factor (from Watts to Amperes) is given by

$$C_{ampere} = \frac{e\lambda_0}{hc} (A/W), \quad (28)$$

where e , h , λ_0 and c are the electron charge, the Planck's constant, the speed of light and the laser wavelength, respectively.

2) *Noise Limit Sensitivity of Optical Module*: Shot noise is a type of readout noise in experimental observation. When the number of energy-carrying particles (such as electrons in a circuit or photons in an optical instrument) in the observation

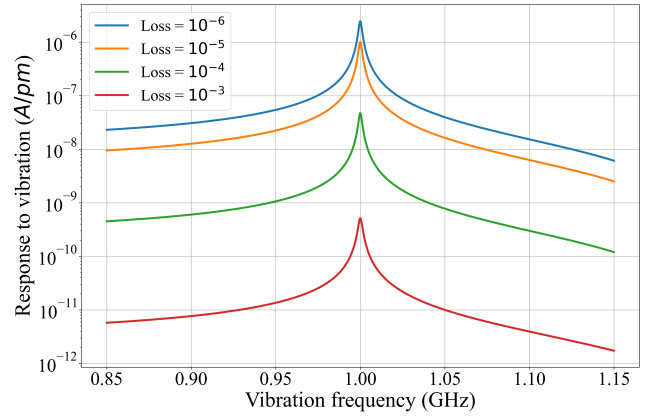


Fig. 9. The response to mirror vibration with respect to carrier frequency.

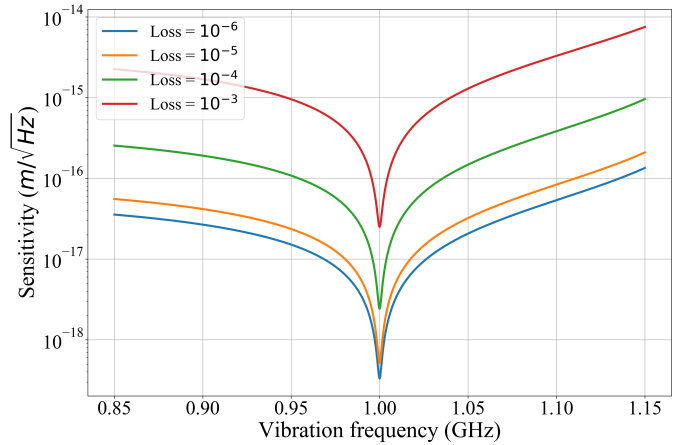


Fig. 10. The noise limited sensitivity.

is small enough to cause observable statistical fluctuations in data reading, the statistical readout fluctuations are called shot noise. Uncertainty of quantum noise and optical radiation pressure noise is described in Section III-D3. It is reported that the noise limited sensitivity at low frequencies (a few tens of Hertz) can reach up to 10^{-23} m/ $\sqrt{\text{Hz}}$, which size is several kilometers [31]. This simulation shows the noise limited sensitivity of the proposed optical module at higher frequencies and smaller size. As shown in Figure 10, the highest sensitivity occurs at the resonant frequency 1 GHz. Similarly, the detection sensitivity and power loss coefficient are negatively correlated.

V. SYSTEM PERFORMANCE EVALUATION

A. Gain from Low Noise Amplifier

We evaluate the link performance via employing a low noise amplifier (LNA) in the system. Assume that the input signal power spectral density is s_I . The next level has certain noise n_{xx} . The system SNR without LNA is given by

$$\text{SNR}_f = \frac{s_I}{n_I + n_{xx}}. \quad (29)$$

TABLE II
PARAMETERS USED IN FINESSE SIMULATION

Parameter	Value
east end mirror transmissivity	5×10^{-6}
east end mirror power loss	1×10^{-5}
east incident mirror transmissivity	0.014
east incident mirror loss	1×10^{-5}
north end mirror transmissivity	5×10^{-6}
north end mirror power loss	1×10^{-5}
north incident mirror transmissivity	0.014
north incident mirror power loss	1×10^{-5}
beam splitter mirror transmissivity	0.5
beam splitter mirror reflectivity	0.5
north arm length	7.5 cm
east arm length	7.5 cm
laser power	1 W
wavelength	1064 nm

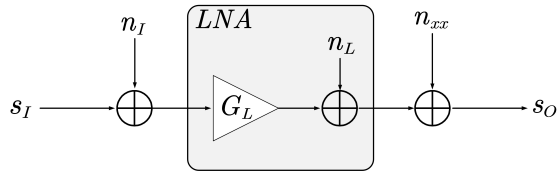


Fig. 11. The signal flow graph of the receiver system with an LNA.

Then, we introduce an LNA with noise n_L and gain $G_L > 1$, as shown in Figure 11. The system SNR at the LNA output can be given by

$$\text{SNR}_f^L = \frac{G_L s_I}{G_L n_I + n_L + n_{xx}}. \quad (30)$$

The SNR gain from LNA is given as follows

$$\text{SNR}_f^L - \text{SNR}_f = \frac{s_I [(G_L - 1) n_{xx} - n_L]}{(G_L n_I + n_L + n_{xx})(n_I + n_{xx})}. \quad (31)$$

When $G_L > G_L^* = n_L/n_{xx} + 1$, the LNA will improve the SNR of the system.

B. System Sensitivity

The system link simulation diagram is shown in Figure 12. The OOK modulation signal is transmitted to the resonant circuit, consisted of inductor and piezoelectric film. Then, the RF signal excites the piezoelectric film to vibrate, leading the variation of light phase in the optical module. Finally, the photodetector transfers the light signal to electric signal for symbol detection. Detailed parameters used in the simulation are shown in Table III.

For the OOK modulation, the carrier frequency is set to 1 GHz and assume the bandwidth is 1 kHz. We set the LNA gain to be a typical value $G_L = 30$ dB [39]. The electrical signal excites the piezoelectric film to vibrate through a coupling circuit, where the response signal is characterized in Section III-C. This process also introduces equivalent film thermal noise in Section III-D2, whose noise power spectral density

TABLE III
TYPICAL PARAMETERS USED IN SYSTEM LINK SIMULATION

Name	Symbol	Value
environment temperature	T	300 K
carrier frequency	f_c	1 GHz
signal bandwidth	BW	1 kHz
modulation method	MM	OOK
LNA gain	G_L	30 dB
LNA noise temperature	T_L	25 K
LC circuit noise PSD	n_{LC}	8.3×10^{-21} V ² /Hz
film noise PSD	n_f	3.4×10^{-55} m ² /Hz
Note: PSD represents power spectral density, whose units for electric and displacement signals are V ² /Hz and m ² /Hz, respectively.		

is $n_f = 3.4 \times 10^{-55}$ m²/Hz. Assuming that the lens power loss is 1×10^{-5} , the noise characterization of the POEMS with contributions from circuit Johnson noise (green), optical noise (orange), film thermal noise (blue) and wireless channel noise (red) are shown in Figure 13. It can be seen that the signal can be differentiated from the noise.

According to the theoretical analysis in Section III, the system sensitivity critically depends on the optical module detection sensitivity and channel bandwidth, while the detection sensitivity depends on the lens power loss coefficient. Figure 14 and Figure 15 show the system sensitivity variation with the signal bandwidth under different loss coefficients. Assuming that the power loss coefficient is 1×10^{-5} , for system with LNA, the system sensitivity at bandwidths 3.75 kHz and 5 MHz are -152.3 dBm and -116.6 dBm, respectively. Lower bandwidth and lower power loss coefficient lead to higher sensitivity.

In Appendix A-A, we summarize the reference sensitivity power levels of evolved universal terrestrial radio access (E-UTRA) base station and narrowband internet of thing (NB-IoT) base station in 4G LTE system. The highest sensitivities for NB-IoT and E-UTRA base stations are -133.7 dBm at bandwidth 3.75 kHz and -101.5 dBm at bandwidth 5 MHz, respectively. It shows that about 18 dB at bandwidth 3.75 kHz and 15 dB at bandwidth 5 MHz gain can be predicted by this prototype design with LNA. Also, we calculate the equivalent sensitivity of atom-based system in Appendix A-B, which is about -120 dBm at bandwidth 1 Hz. For a fair comparison, we normalize the bandwidth to be 3.75 kHz and compare it with proposed system without LNA. The proposed prototype design can obtain a gain of 40 dB.

C. Signal to Noise Ratio, Bit Error Rate and Capacity

Figure 16 shows the system output SNR with external wireless channel noise power. When the signal power is -150 dBm and the wireless channel noise power is -160 dBm, more than 7 dB SNR can be achieved.

We refer to IM/DD Gaussian channel capacity under vector modulation, to evaluate the achievable rate of the proposed piezo-opto-electro-mechanical system [40]. Assuming wireless channel noise power is -165 dBm, we get upper and lower bounds on the channel capacity results under different received power, as shown in Figure 17.

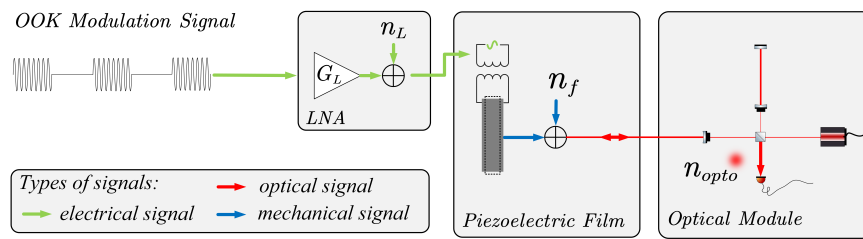


Fig. 12. The signal flow graph in the system link simulation.

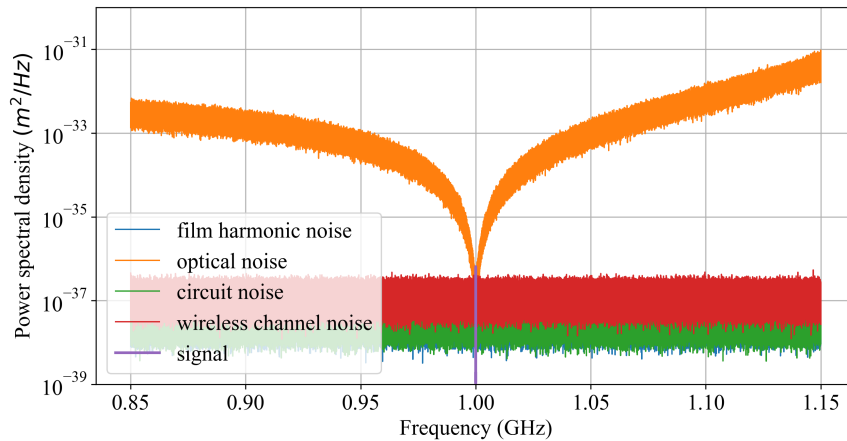


Fig. 13. Signal and noises power spectral densities with input power -160 dBm.

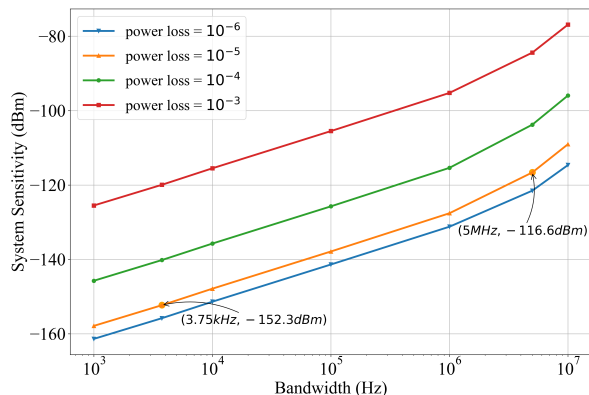


Fig. 14. The system sensitivity to different bandwidths and lens power loss coefficients with LNA in consideration. The bandwidth varies from 1 kHz to 10 MHz.

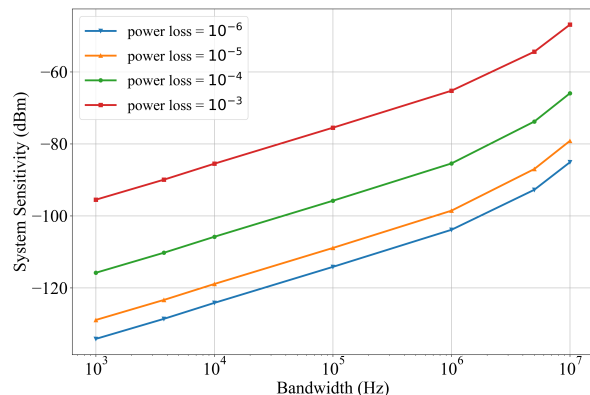


Fig. 15. The system sensitivity to different bandwidths and lens power loss coefficients without LNA in consideration. The bandwidth varies from 1 kHz to 10 MHz.

Under different input power and wireless channel noise power, we perform the bit error rate simulation of the 1 kbps OOK signal, as shown in Figure 18. The BER is lower than 10^{-3} when the received power is -150 dBm and the wireless channel noise power is lower than -175 dBm.

VI. CONCLUSION

We have proposed a high sensitivity piezo-opto-electro-mechanical receiver system, which utilizes optical module to detect the piezoelectric film vibration driven by RF signal. Based on the analysis of piezoelectric vibration and optical

response to the vibration, we have analyzed the system transfer function in the frequency domain. Both theoretical results and numerical/simulation results are provided to test the feasibility of the proposed system. For OOK modulation signal with 5 MHz bandwidth and 1 GHz carrier frequency, the system receiving sensitivity can be predicted to -118.9 dBm, which significantly outperforms that of the reference sensitivity power of the evolved universal terrestrial radio access base stations. The preliminary experiment confirm the accuracy of AIN film susceptibility analysis and infer a -6 dB gain to predicted system sensitivity. Future works include the

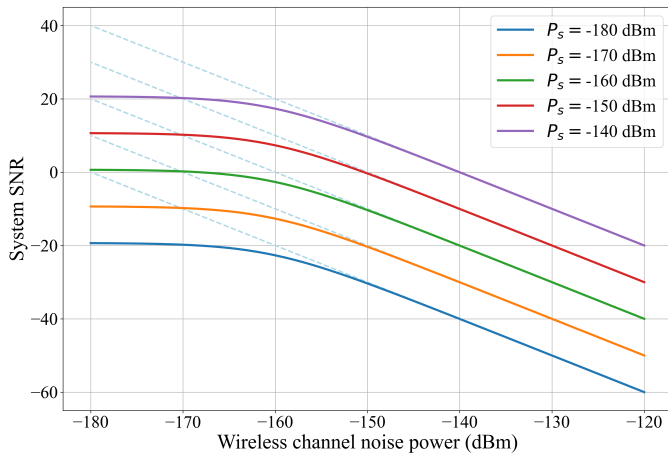


Fig. 16. The SNR of the output signal from optical detection under different wireless channel noise power.

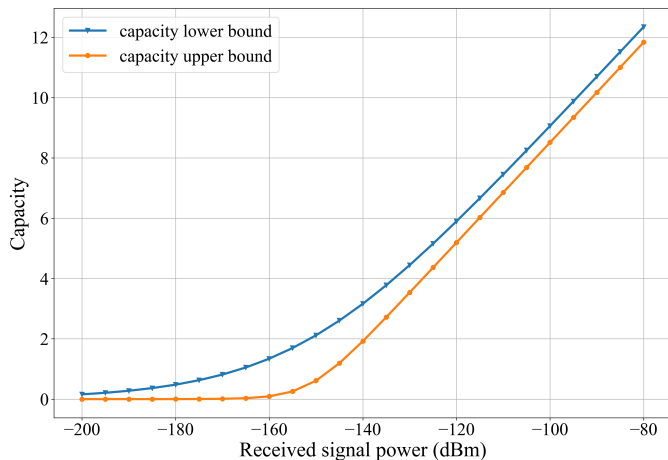


Fig. 17. Upper and lower bounds on the capacity of the system under consideration.

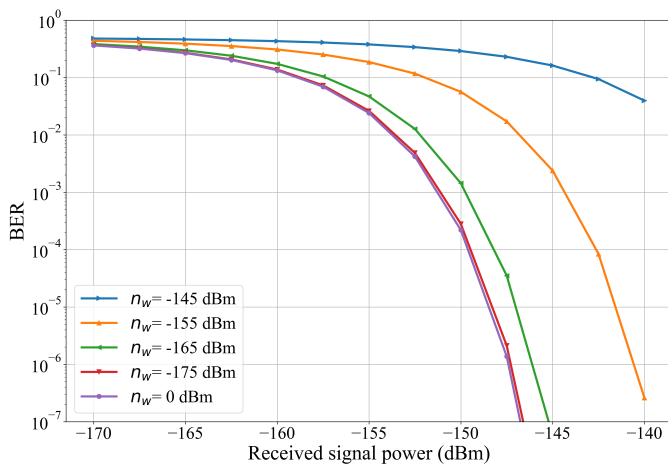


Fig. 18. The bit error rate under different wireless channel noise power level.

fabrication of the proposed architecture, and the test in various laboratory and practical scenarios.

APPENDIX A REFERENCE SENSITIVITY POWER LEVEL

A. System Sensitivity of Communication Base Stations

The reference sensitivity power level $P_{REFSENS}$ is the minimum mean power received at the antenna connector at which a throughput requirement shall be met for a specified reference measurement channel. For evolved universal terrestrial radio access (E-UTRA), the throughput shall be larger than or equal to 95% of the maximum throughput of the reference measurement channel. The reference sensitivity power levels for Wide Area Base Station (BS), Local Area BS, Home BS and Medium Range BS are shown in Table IV [35].

For narrowband internet of thing (NB-IoT) standalone BS or E-UTRA BS with NB-IoT (in-band and/or guard band), NB-IoT throughput shall be larger than or equal to 95% of the maximum throughput of the reference measurement channel. The reference sensitivity power levels for Wide Area BS, Local Area BS, Home BS and Medium Range BS are shown in Table V [35].

B. System Sensitivity of Atom-Based Sensing System

Atom-based measurements have been successfully utilized for magnetometry, time and frequency standards, inertial force sensing as well as searches for local Lorentz invariance and intrinsic electric dipole moments of the neutron and electron, amongst others [41]. It is reported that absolute RF electric field sensing is $E_{min} = 5 \mu Vcm^{-1}Hz^{-1/2}$. The radiation electric field is from a horn antenna, driven by an RF generator. We calculate the equivalent RF generator output signal power as its system sensitivity with power unit Watt.

Assuming that RF generator output signal power is P_{out} , effective radiation area is $A = 1cm^2$, antenna gain is $G_A = 15$ dB and bandwidth is $B = 1$ Hz, the electric field strength sensed by the atom system is given by

$$E_0 = \sqrt{\frac{2\langle|\vec{S}|\rangle}{\epsilon_0 c B}}, \quad (32)$$

where $\langle|\vec{S}|\rangle = G_A P_{out}/A$ is the energy flow density of electromagnetic wave, ϵ_0 is the vacuum dielectric constant and c is the speed of light, respectively.

According to the electric field sensing sensitivity $E_{min} = 5 \mu Vcm^{-1}Hz^{-1/2}$, the system sensitivity in the form of power is given by

$$P_{min} = \frac{A}{2G_A} \epsilon_0 c E_{min}^2 B \approx 1 \times 10^{-15} W = -120 \text{ dBm}. \quad (33)$$

APPENDIX B PROOF OF LEMMAS AND THEOREMS

A. Proof of Theorem 1

Considering the separation of variables, i.e., $u(z, t) = Z(z) \cdot e^{j\omega t}$, and defining the phase velocity $v_a \triangleq \sqrt{\frac{cD}{\rho}}$ of

TABLE IV
REFERENCE SENSITIVITY POWER LEVELS IN EUTRA BASE STATIONS.

Base station types	Bandwidth [MHz]	Reference sensitivity power level [dBm]
Wide Area Base Station	5	-101.5
Local Area Base Station	5	-93.5
Home Base Station	5	-93.5
Medium Range a Base Station	5	-96.5

Note: The reference measurement channel is specified in Annex A1-3 in [35].

TABLE V
REFERENCE SENSITIVITY POWER LEVELS IN NB-IoT BASE STATIONS.

Base station types	Bandwidth [kHz]	Reference sensitivity power level [dBm]
Wide Area Base Station	3.75	-133.3
Local Area Base Station	3.75	-125.3
Home Base Station	3.75	-125.3
Medium Range a Base Station	3.75	-128.3

Note: The reference measurement channel is specified in Annex A14-2 in [35].

the vibration module along the z-axis, the wave equation $Z(z)$ is given as follows,

$$\begin{aligned} \omega^2 Z + \frac{c^D}{\rho} \frac{d^2 Z}{dz^2} &= 0, \\ \frac{d^2 Z}{dz^2} + \frac{\omega^2}{c_v^2} Z &= 0, \end{aligned} \quad (34)$$

whose formal solution is

$$Z(z) = A \sin(\beta z) + B \cos(\beta z), \quad (35)$$

where $\beta = \omega/v_a$ is the amplitude of the wave vector.

According to Maxwell equation $\nabla \cdot D = \rho_{free} = 0$, the electric displacement vector is a variable only depends on time, $D(z, t) = D(t) = D_0 e^{j\omega t}$. Substituting boundary condition $T|_{z=0} = T|_{z=L_T} = 0$ into the solution, then we can get that $A = e_{33} D_0 / (\varepsilon^S c^D \beta)$ and $B = A [\cos(\beta L_T) - 1] / (\sin(\beta L_T))$. A complete solution can be given by

$$u(z, t) = \frac{e_{33} D_0}{\varepsilon^S c^D \beta} \frac{\cos(\beta(L_T - z)) - \cos(\beta z)}{\sin(\beta L_T)} e^{j\omega t}. \quad (36)$$

The surface vibration at $z = L_T$ is given by

$$\begin{aligned} u(L_T, t) &= \frac{e_{33} D_0}{\varepsilon^S c^D \beta} \frac{1 - \cos(\beta L_T)}{\sin(\beta L_T)} e^{j\omega t}, \\ &= \frac{e_{33} D_0}{\varepsilon^S c^D \beta} \tan\left(\frac{\beta L_T}{2}\right) e^{j\omega t}. \end{aligned} \quad (37)$$

Integrate the electric field E in the z direction to obtain the expression of the electric potential as follows

$$\begin{aligned} V &= V_0 \cdot e^{j\omega t} \\ &= \int_0^{L_T} E(z, t) dz = \int_0^{L_T} \frac{1}{\varepsilon^S} (D - eS) dz \\ &= \frac{DL_T}{\varepsilon^S} - \frac{e_{33}}{\varepsilon^S} (u(L_T, t) - u(0, t)) \\ &= \left\{ \frac{D_0 L_T}{\varepsilon^S} - \frac{e_{33}}{\varepsilon^S} [u(L_T, 0) - u(0, 0)] \right\} \cdot e^{j\omega t} \\ &= \left[\frac{D_0 L_T}{\varepsilon^S} - \frac{2e_{33}^2 D_0}{(\varepsilon^S)^2 c^D \beta} \tan\left(\frac{\beta L_T}{2}\right) \right] \cdot e^{j\omega t}, \end{aligned} \quad (38)$$

It is easy to obtain the expression of D_0 as follows

$$D_0 = \frac{V_0 \beta \varepsilon^S}{\beta L_T - 2k_t^2 \tan(\beta L_T / 2)}, \quad (39)$$

where $k_t^2 = e_{33}^2 / (c^D \varepsilon^S)$ is electromechanical coupling coefficient, a parameter that characterizes the properties of piezoelectric films.

Ideally, the series resonance condition corresponds to zero input impedance. The input impedance for thickness excitation case is

$$Z_{in} = \frac{1}{j\omega C_0} (1 - k_t^2 \frac{\tan(\beta L_T / 2)}{\beta L_T / 2}), \quad (40)$$

where $C_0 = LW\varepsilon^S / L_T$ is the static capacitance of piezoelectric film [33]. When $Z_{in} = 0$, resonance frequency ω_s should satisfy

$$\begin{aligned} k_t^2 \tan(\beta L_T / 2) &= \beta L_T / 2, \\ \omega_s &= \beta v_a. \end{aligned} \quad (41)$$

Near the first pole, the tangent function can be approximated as

$$\tan\left(\frac{\beta L_T}{2}\right) \approx \frac{4\beta L_T}{\pi^2 - (\beta L_T)^2} = \frac{\beta L_T}{2k_t^2}. \quad (42)$$

According to Eq. 41 and Eq. 42, the series resonance frequency is given by

$$\omega_s = \frac{v_a}{L_T} \sqrt{\pi^2 - 8k_t^2}. \quad (43)$$

B. Proof of Theorem 2

Considering the separation of variables, i.e., $v(z, t) = V(z) \cdot e^{j\omega t}$, the wave equation $V(z)$ is given as follows,

$$c^D \frac{d^2 V}{dz^2} + j\omega \eta \frac{dV}{dz} = -\rho \omega^2 V, \quad (44)$$

and the formal solution is

$$V(z) = A \sin(\hat{\beta} z) + B \cos(\hat{\beta} z), \quad (45)$$

where $\hat{\beta} = \beta / \sqrt{1 + j\omega \eta / c^D} \approx \beta (1 - j / (2Q))$ under the condition for first-order approximation; and the quality factor

$Q = c^D/(\eta\omega)$. According to Eq. (37), the surface vibration at $z = L_T$ is given by

$$u(L_T, t) = \frac{e_{33}D_0}{\varepsilon^S c^D \hat{\beta}} \tan\left(\frac{\hat{\beta}L_T}{2}\right) \cdot e^{j\omega t}. \quad (46)$$

According to Eq. (39), the amplitude of electric displacement vector is approximated as

$$D_0 = \frac{V_0 \varepsilon^S}{L_T} \frac{1}{1 - k_t^2 \frac{\tan(\hat{\beta}L_T/2)}{\hat{\beta}L_T/2}}. \quad (47)$$

Based on the series resonance condition as shown in Eq. 43, the approximate result is as follows

$$\begin{aligned} \tan\left(\frac{\hat{\beta}L_T}{2}\right) &\approx \frac{\tan\left(\frac{\beta L_T}{2}\right) - \tan\left(j\frac{1}{2Q}\frac{\beta L_T}{2}\right)}{1 + \tan\left(\frac{\beta L_T}{2}\right)\tan\left(j\frac{1}{2Q}\frac{\beta L_T}{2}\right)} \\ \frac{\tan\left(\frac{\hat{\beta}L_T}{2}\right)}{\hat{\beta}L_T/2} &\approx \frac{\frac{\beta L_T}{2} \left(1 - j\frac{1}{2Q}\right)}{x \left(\frac{1}{k_t^2} - j\frac{1}{2Q}\right)} \\ &\approx \frac{x \left(\frac{1}{k_t^2} - j\frac{1}{2Q}\right)}{1 + j\frac{1}{k_t^2}\frac{1}{2Q}x^2} \cdot \frac{1}{x \left(1 - j\frac{1}{2Q}\right)} \\ &\approx \frac{1}{k_t^2} \frac{1}{1 + j\frac{1}{k_t^2}\frac{1}{2Q}x^2} \\ &= \frac{1}{k_t^2 + j\frac{x^2}{2Q}}, \end{aligned} \quad (48)$$

where $x = \beta L_T/2$ and $\beta L_T/(4Q) \ll 1$.

Substitute Eq. 48 into Eq. 47 and Eq. 46, the amplitude of electrical displacement vector is

$$D_0 \approx \frac{V \varepsilon^S / L_T}{1 - \frac{k_t^2}{k_t^2 + j\frac{x^2}{2Q}}} = \frac{V \varepsilon^S}{L_T} \left(1 - j\frac{8Qk_t^2}{\pi^2 - 8k_t^2}\right), \quad (49)$$

and the surface vibration equation is

$$\begin{aligned} u(L_T, t) &= \frac{e_{33}D_0}{\varepsilon^S c^D \hat{\beta}} \tan\left(\frac{\hat{\beta}L_T}{2}\right) \cdot e^{j\omega t} \\ &= \frac{e_{33}D_0 L_T}{2\varepsilon^S c^D} \frac{\tan\left(\frac{\hat{\beta}L_T}{2}\right)}{\frac{\hat{\beta}L_T}{2}} \cdot e^{j\omega t} \\ &\approx \frac{e_{33}L_T}{2\varepsilon^S c^D} \cdot \frac{V_0 \varepsilon^S}{L_T} \left(1 - j\frac{8Qk_t^2}{\pi^2 - 8k_t^2}\right) \cdot \frac{1}{k_t^2 + j\frac{\pi^2 - 8k_t^2}{8Q}} \cdot e^{j\omega t} \\ &= \frac{V_0 e_{33}}{2c^D k_t^2} \cdot \frac{1 - j\frac{8Qk_t^2}{\pi^2 - 8k_t^2}}{1 + j\frac{\pi^2 - 8k_t^2}{8Qk_t^2}} \cdot e^{j\omega t} \\ &\approx -j\frac{4QV_0 e_{33}}{c^D \pi^2} \cdot e^{j\omega t}. \end{aligned} \quad (50)$$

C. Proof of Theorem 3

Assuming that $r = t = 1/\sqrt{2}$ and the phase difference of reflection and transmission can be ignored, the output electric

field can be given by

$$\begin{aligned} \mathbf{E}_{\text{out}} &= \frac{1}{2} \mathbf{E}_0 \left(e^{i(\Phi_1 + 2k_0 x_m)} + e^{i\Phi_2} \right) \\ &= \frac{1}{2} \mathbf{E}_0 \left(e^{i(-2k_0 L_N)} (1 + i2k_0 a_s \cos(\omega_s t + \varphi_s)) \right. \\ &\quad \left. + e^{i(-2k_0 L_E)} \right). \end{aligned} \quad (51)$$

Define the common and differential arm lengths as $\bar{L} = \frac{L_N + L_E}{2}$ and $\Delta L = L_N - L_E$. Noticed the fact that light power P is proportional to the square of electric field amplitude $|E_0|^2$, the output light power will be as follows,

$$\begin{aligned} P_{\text{out}} &= \frac{\mathbf{E}_{\text{out}} \mathbf{E}_{\text{out}}^*}{\mathbf{E}_0 \mathbf{E}_0^*} P_0 \\ &= P_0 \left[\cos(k_0 \Delta L) + k_0 a_s \cos(\omega_s t + \varphi_s) e^{i(k_0 \Delta L - \pi/2)} \right] \\ &\quad \left[\cos(k_0 \Delta L) + k_0 a_s \cos(\omega_s t + \varphi_s) e^{i(k_0 \Delta L - \pi/2)} \right]^* \\ &= P_0 \left[\cos^2(k_0 \Delta L) + k_0 a_s \sin(2k_0 \Delta L) \cos(\omega_s t + \varphi_s) \right. \\ &\quad \left. + k_0^2 a_s^2 \cos^2(\omega_s t + \varphi_s) \right]. \end{aligned} \quad (52)$$

The output current of photodetector is given by

$$\begin{aligned} I_{\text{out}} &= \alpha P_0 \left[\cos^2(k_0 \Delta L) + k_0 a_s \sin(2k_0 \Delta L) \cos(\omega_s t + \varphi_s) \right. \\ &\quad \left. + k_0^2 a_s^2 \cos^2(\omega_s t + \varphi_s) \right]. \end{aligned} \quad (53)$$

D. Proof of Theorem 4

Firstly, we use G_{PRM} and G_{SRM} characterise the gain of power cycling cavity and signal cycling cavity in Figure 6. Then, we can simplify the module to be a Michelson interferometer with two arm cavities, which injection field $\mathbf{E}_1 = G_{PRM} \mathbf{E}_0$ and output field $\mathbf{E}_S = \mathbf{E}_{\text{out}}/G_{SRM}$.

Secondly, we analyse the input-output relationship of a two mirror cavity with $ITMN(r_1, t_1)$, $ETMN(r_2, t_2)$ and length L_N , the electric field can be given as follows,

$$\begin{aligned} \mathbf{E}_3 &= t_1 \mathbf{E}_2 + r_1 \mathbf{E}'_3, \\ \mathbf{E}'_3 &= r_2 \mathbf{E}_3 e^{-i2k_0 L_N} e^{i2k_0 x_m}, \\ \mathbf{E}'_2 &= r_1 \mathbf{E}_2 + t_1 \mathbf{E}'_3. \end{aligned} \quad (54)$$

The output field \mathbf{E}'_2 is given by

$$\mathbf{E}'_2 = \mathbf{E}_2 \left(r_1 - \frac{r_2 t_1^2 e^{-i2k_0 L_N}}{e^{-i2k_0 x_m} - r_1 r_2 e^{-i2k_0 L_N}} \right), \quad (55)$$

where r_1 , t_1 , r_2 and t_2 are the reflection coefficient, transmission coefficient of mirror $ITMN$, and the reflection coefficient, transmission coefficient of mirror $ETMN$, respectively.

Similarly, the output field \mathbf{E}'_4 of east arm can be given by

$$\mathbf{E}'_4 = \mathbf{E}_4 \left(r_3 - \frac{r_4 t_3^2 e^{-i2k_0 L_E}}{1 - r_3 r_4 e^{-i2k_0 L_E}} \right), \quad (56)$$

where r_3 , t_3 , r_4 and t_4 are the reflection coefficient, transmission coefficient of mirror $ITME$, and the reflection coefficient, transmission coefficient of mirror $ETME$, respectively.

Finally, assuming that $r = t = 1/\sqrt{2}$ and the phase difference of reflection and transmission can be ignored, the output electric field can be given by

$$\begin{aligned}
\mathbf{E}_{\text{out}} &= \mathbf{E}_S G_{SRM} \\
&= (r\mathbf{E}_4' + t\mathbf{E}_2') G_{SRM} \\
&= G_{SRM} \left[\mathbf{E}_4 \left(r_3 - \frac{r_4 t_3^2 e^{-i2k_0 L_E}}{1 - r_3 r_4 e^{-i2k_0 L_E}} \right) \right. \\
&\quad \left. + \mathbf{E}_2 \left(r_1 - \frac{r_2 t_1^2 e^{-i2k_0 L_N}}{e^{-i2k_0 x_m} - r_1 r_2 e^{-i2k_0 L_N}} \right) \right] \\
&= \frac{1}{\sqrt{2}} G_{PRM} G_{SRM} \mathbf{E}_0 \left[\left(r_3 - \frac{r_4 t_3^2 e^{-i2k_0 L_E}}{1 - r_3 r_4 e^{-i2k_0 L_E}} \right) \right. \\
&\quad \left. + \left(r_1 - \frac{r_2 t_1^2 e^{-i2k_0 L_N}}{e^{-i2k_0 x_m} - r_1 r_2 e^{-i2k_0 L_N}} \right) \right]. \tag{57}
\end{aligned}$$

In this work, we choose symmetry parameters for two arm cavities, $r_1 = r_3$, $r_2 = r_4$, $t_1 = t_3$ and $t_2 = t_4$. In order to obtain high sensitivity, the reflection coefficient r_1, r_2 approximately equal to 1 and $t_1, t_2 \ll 1$. The output current is given by

$$\begin{aligned}
I_{\text{out}} &= \frac{1}{2} G_{PRM}^2 G_{SRM}^2 P_0 \left| \left(1 - \frac{t_3^2 e^{-i2k_0 L_N}}{1 - e^{-i2k_0 L_N}} \right) \right. \\
&\quad \left. + \left(1 - \frac{t_1^2 e^{-i2k_0 L_N}}{e^{-i2k_0 x_m} - e^{-i2k_0 L_N}} \right) \right|^2. \tag{58}
\end{aligned}$$

E. Proof of Theorem 5

Hamiltonian in classical form of POEMS is given by [1]

$$\begin{aligned}
H &= \frac{p^2}{2m} + \frac{m\omega_M^2 x^2}{2} + \frac{\phi^2}{2L} + \frac{q^2}{2C(x)} + \\
&\quad 2g\sqrt{\frac{m\omega_M}{C(x)\omega_{LC}}} xq - qV. \tag{59}
\end{aligned}$$

Under resonance condition, $\omega_M = \omega_{LC} = \omega_r$. The canonical equations are given as follows,

$$\begin{aligned}
\frac{\partial H}{\partial p} &= \dot{x}, \\
\frac{\partial H}{\partial x} &= -\dot{p}, \tag{60}
\end{aligned}$$

and

$$\begin{aligned}
\dot{p} &= -\frac{\partial H}{\partial x} \\
&= -m\omega_r^2 x - \frac{q^2}{2} \frac{\partial}{\partial x} \left(\frac{1}{C(x)} \right) - 2g\sqrt{m} \frac{\partial}{\partial x} \left(\frac{x}{\sqrt{C(x)}} \right) q, \\
\dot{\phi} &= -\frac{\partial H}{\partial q}, \\
&= -\frac{q}{C(x)} - 2g\sqrt{m} \frac{x}{\sqrt{C(x)}} + V. \tag{61}
\end{aligned}$$

Assuming a real system with random disturbance, the Langevin Equations are given by

$$\begin{aligned}
\dot{x} &= \frac{p}{m}, \\
\dot{p} &= -m\omega_r^2 x - \frac{q^2}{2} \frac{\partial}{\partial x} \left(\frac{1}{C(x)} \right) - 2g\sqrt{m} \frac{\partial}{\partial x} \left(\frac{x}{\sqrt{C(x)}} \right) q \\
&\quad - \Gamma_m p - F, \\
\dot{q} &= \frac{\phi}{L}, \\
\dot{\phi} &= -\frac{q}{C(x)} - 2g\sqrt{m} \frac{x}{\sqrt{C(x)}} - \Gamma_{LC} \phi + V, \tag{62}
\end{aligned}$$

where m and L_{LC} are equivalent mass of piezoelectric oscillator and inductance in the resonant circuit, respectively; ω_m and ω_{LC} are resonance frequencies of oscillator and LC circuit, respectively; Γ_m and Γ_{LC} are the damping coefficients of the piezoelectric film and the LC resonant circuit, respectively; and G is the coupling coefficient.

Assume that the equivalent force of the thermal motion δF_{th} is the only force. The first order perturbation equations around the equilibrium point $\bar{x} = \bar{p} = \bar{q} = \bar{\phi} = 0$, are as follows,

$$\begin{aligned}
\delta \dot{x} &= \frac{\delta p}{m}, \\
\delta \dot{p} &= -m\omega_r^2 \delta x - \frac{\bar{q}^2}{2} \frac{\partial^2}{\partial x^2} \left(\frac{1}{C(x)} \right)_{x=\bar{x}} \delta x \\
&\quad - \bar{q} \frac{\partial}{\partial x} \left(\frac{1}{C(x)} \right)_{x=\bar{x}} \delta q - 2\bar{q}g\sqrt{m} \frac{\partial^2}{\partial x^2} \left(\frac{x}{\sqrt{C(x)}} \right)_{x=\bar{x}} \delta x \\
&\quad - 2g\sqrt{m} \frac{\partial}{\partial x} \left(\frac{x}{\sqrt{C(x)}} \right)_{x=\bar{x}} \delta q - \Gamma_m \delta p - \delta F_{th}, \\
\delta \dot{q} &= \frac{\delta \phi}{L}, \\
\delta \dot{\phi} &= -\frac{\delta q}{C(\bar{x})} - \bar{q} \frac{\partial}{\partial x} \left(\frac{1}{C(x)} \right)_{x=\bar{x}} \delta x \\
&\quad - 2g\sqrt{m} \frac{\partial}{\partial x} \left(\frac{x}{\sqrt{C(x)}} \right)_{x=\bar{x}} \delta x - \Gamma_{LC} \delta \phi + \delta V. \tag{63}
\end{aligned}$$

Transforming the analysis from time domain to frequency domain, we can get the equations as follows,

$$\begin{aligned}
-i\Omega \delta x(\Omega) &= \frac{\delta p(\Omega)}{m}, \\
-i\Omega \delta p(\Omega) &= -m\omega_r^2 \delta x(\Omega) - 2g\sqrt{\frac{m}{C(\bar{x})}} \delta q(\Omega) \\
&\quad - \Gamma_m \delta p(\Omega) - \delta F_{th}(\Omega), \\
-i\Omega \delta q(\Omega) &= \frac{\delta \phi(\Omega)}{L}, \\
-i\Omega \delta \phi(\Omega) &= -\frac{\delta q(\Omega)}{C(\bar{x})} - 2g\sqrt{\frac{m}{C(\bar{x})}} \delta x(\Omega) \\
&\quad - \Gamma_{LC} \delta \phi(\Omega) + \delta V(\Omega). \tag{64}
\end{aligned}$$

Redefine the coupling coefficient $G = 2g\sqrt{\frac{m}{C(\bar{x})}} = 2g\sqrt{\frac{mL_T}{\epsilon^S W L}}$,

the equations in frequency domain are given as follows,

$$\begin{aligned}
-i\Omega\delta x(\Omega) &= \frac{\delta p(\Omega)}{m}, \\
-i\Omega\delta p(\Omega) &= -m\omega_r^2\delta x(\Omega) - \Gamma_m\delta p(\Omega) - G\delta q(\Omega) - \delta F_{th}(\Omega), \\
-i\Omega\delta q(\Omega) &= \frac{\delta\phi(\Omega)}{L}, \\
-i\Omega\delta\phi(\Omega) &= -\frac{\delta q(\Omega)}{C(\bar{x})} - \Gamma_{LC}\delta\phi(\Omega) - G\delta x(\Omega) + \delta V(\Omega).
\end{aligned} \tag{65}$$

According to the above equation, the response of the system to force or voltage signal excitation can be calculated. For piezoelectric oscillator and LC circuit, two parameters are defined as follows,

$$\begin{aligned}
\chi_m(\Omega) &= \frac{1}{m(\Omega_m^2 - \Omega^2 - i\Omega\Gamma_m)}, \\
\chi_{LC}(\Omega) &= \frac{1}{L(\Omega_{LC}^2 - \Omega^2 - i\Omega\Gamma_{LC})}.
\end{aligned} \tag{66}$$

Again, the equations in frequency domain can be written as follows,

$$\begin{aligned}
\chi_m(\Omega)(-\delta F_{th}(\Omega) + G\chi_{LC}(\Omega)\delta V(\Omega)) \\
= (1 - G^2\chi_m(\Omega)\chi_{LC}(\Omega))\delta x(\Omega), \\
\delta x(\Omega) = (\chi_m(\Omega)^{-1} - G^2\chi_{LC}(\Omega))^{-1} \\
(-\delta F_{th}(\Omega) + G\chi_{LC}(\Omega)\delta V).
\end{aligned} \tag{67}$$

Defining $\chi_m^{eff}(\Omega) \triangleq (\chi_m(\Omega)^{-1} - G^2\chi_{LC}(\Omega))^{-1}$, the transfer function of the system in frequency domain is given by

$$\begin{aligned}
\delta x(\Omega) &= \chi_m^{eff}(-\delta F_{th}(\Omega) + G\chi_{LC}(\Omega)\delta V(\Omega)), \\
\delta\varphi(\Omega) &= 2k\chi_m^{eff}(-\delta F_{th}(\Omega) + G\chi_{LC}(\Omega)\delta V(\Omega)) \\
&\quad + \delta\varphi_{im}(\Omega),
\end{aligned} \tag{68}$$

where $\delta\varphi = 2k\delta x$ ($k = 2\pi/\lambda$) represents the phase variation to δx .

Moreover, considering the light force of the optical cavity in a real system, the expression of $\chi_m(\omega)$ is modified as follows,

$$\begin{aligned}
\chi_{m,eff}^{-1}(\omega) &= \chi_m^{-1}(\omega) + \Sigma(\omega), \\
\Sigma(\omega) &= 2m_{eff}\Omega_m g^2 \left\{ \frac{1}{(\Delta + \omega) + i\kappa/2} + \frac{1}{(\Delta - \omega) - i\kappa/2} \right\},
\end{aligned} \tag{69}$$

where Δ and κ represent the laser detuning to the optical cavity and attenuation coefficient, respectively [18].

Then, we introduce two parameters $\delta\Omega_m$ and Γ_{opt} as follows,

$$\begin{aligned}
\delta\Omega_m(\omega) &= g^2 \frac{\Omega_m}{\omega} \left[\frac{\Delta + \omega}{(\Delta + \omega)^2 + \kappa^2/4} + \frac{\Delta - \omega}{(\Delta - \omega)^2 + \kappa^2/4} \right], \\
\Gamma_{opt}(\omega) &= g^2 \frac{\Omega_m}{\omega} \left[\frac{\kappa}{(\Delta + \omega)^2 + \kappa^2/4} - \frac{\kappa}{(\Delta - \omega)^2 + \kappa^2/4} \right],
\end{aligned} \tag{70}$$

where $\delta\Omega_m$ and Γ_{opt} represent frequency shift and damping coefficient variation caused by light incident, respectively. Substituting them into Eq. (69),

$$\begin{aligned}
\Sigma(\omega) &\equiv m_{eff}\omega [2\delta\Omega_m(\omega) - i\Gamma_{opt}(\omega)], \\
\chi_{m,eff}^{-1}(\omega) &= m_{eff} [\Omega_m^2 + 2\omega\delta\Omega_m(\omega) - \omega^2] \\
&\quad - i\omega m_{eff} [\Gamma_m + \Gamma_{opt}(\omega)].
\end{aligned} \tag{71}$$

Under different cavity attenuation sizes κ , the form of frequency detuning is not exactly the same. The frequency drift introduced by the optical field is called the optical spring effect, which disappears under certain detuning conditions. Moreover, the radiation pressure in the cavity will produce equivalent cooling and amplification effects on the motion of the end mirror (in our system, it is represented by piezoelectric film).

F. Proof of Theorem 6

In our system, the response of piezoelectric film to RF signals can be approximated as a damped harmonic oscillator model. The vibration equation is given by

$$m_{eff} \frac{dx^2(t)}{dt^2} + m_{eff}\Gamma_m \frac{dx(t)}{dt} + m_{eff}\Omega_m^2 x(t) = \eta_{ex}(t). \tag{72}$$

In the equilibrium, the environment exerts a disturbing force η_{ex} on the damped harmonic oscillator. Defining $\eta(t) \triangleq \eta_{ex}(t)/m_{eff}$, the vibration equation is simplified as follows,

$$\frac{dx^2(t)}{dt^2} + \Gamma_m \frac{dx(t)}{dt} + \Omega_m^2 x(t) = \eta(t). \tag{73}$$

According to the white noise hypothesis, $\eta(t)$ satisfies the following equations,

$$\langle \eta(t) \rangle = 0, \quad \langle \eta(t)\eta(\tau) \rangle = 2\alpha\delta(t - \tau). \tag{74}$$

A solution is given by

$$\begin{aligned}
x(t) &= a_{10}e^{\mu_1 t} + a_{20}e^{\mu_2 t} \\
&\quad + \frac{1}{\mu_1 - \mu_2} \int_0^t [e^{\mu_1(t-t')} - e^{\mu_2(t-t')}] \eta(t') dt',
\end{aligned} \tag{75}$$

where μ_1 and μ_2 are the two solutions to $\mu^2 + \Gamma_m\mu + \Omega_m^2 = 0$, respectively. Under weak stationary condition, the correlation function of simple harmonic noise is given by [42]

$$\langle x(t)x(\tau) \rangle = \frac{\alpha}{\mu_1^2 - \mu_2^2} \left[\frac{1}{\mu_1} e^{\mu_1|t-\tau|} - \frac{1}{\mu_2} e^{\mu_2|t-\tau|} \right]. \tag{76}$$

Fourier transform is applied to the above equation to obtain the simple harmonic noise power spectrum as follows,

$$S(\omega) = 2\alpha_{ex} |\chi_m(\omega)|^2, \tag{77}$$

where $\alpha_{ex} = \alpha m_{eff}^2$ represents the noise strength.

REFERENCES

- [1] T. Bagci, A. Simonsen, S. Schmid, L. G. Villanueva, E. Zeuthen, J. Appel, J. M. Taylor, A. Sørensen, K. Usami, A. Schliesser, *et al.*, “Optical detection of radio waves through a nanomechanical transducer,” *Nature*, vol. 507, no. 7490, pp. 81–85, 2014.
- [2] T. Lv, Z. Lin, P. Huang, and J. Zeng, “Optimization of the energy-efficient relay-based massive iot network,” *IEEE Internet of Things Journal*, vol. 5, no. 4, pp. 3043–3058, 2018.
- [3] K. Miyanabe, T. Gama Rodrigues, Y. Lee, H. Nishiyama, and N. Kato, “An internet of things traffic-based power saving scheme in cloud-radio access network,” *IEEE Internet of Things Journal*, vol. 6, no. 2, pp. 3087–3096, 2019.
- [4] A. Ikpehai, B. Adebisi, K. M. Rabie, K. Anoh, R. E. Ande, M. Ham-moudeh, H. Gacanin, and U. M. Mbanaso, “Low-power wide area network technologies for internet-of-things: A comparative review,” *IEEE Internet of Things Journal*, vol. 6, no. 2, pp. 2225–2240, 2019.
- [5] Q. Du, H. Song, and X. Zhu, “Social-feature enabled communications among devices toward the smart iot community,” *IEEE Communications Magazine*, vol. 57, no. 1, pp. 130–137, 2019.
- [6] S. Gao, X. Zhang, C. Du, and Q. Ji, “A multichannel low-power wide-area network with high-accuracy synchronization ability for machine vibration monitoring,” *IEEE Internet of Things Journal*, vol. 6, no. 3, pp. 5040–5047, 2019.
- [7] L. Feltrin, G. Tsoukaneri, M. Condoluci, C. Buratti, T. Mahmoodi, M. Dohler, and R. Verdone, “Narrowband iot: A survey on downlink and uplink perspectives,” *IEEE Wireless Communications*, vol. 26, no. 1, pp. 78–86, 2019.
- [8] C. Regal and K. Lehnert, “From cavity electromechanics to cavity optomechanics,” in *Journal of Physics: Conference Series*, vol. 264, no. 1. IOP Publishing, 2011, p. 012025.
- [9] A. H. Safavi-Naeini and O. Painter, “Proposal for an optomechanical traveling wave phonon–photon translator,” *New Journal of Physics*, vol. 13, no. 1, p. 013017, 2011.
- [10] J. M. Taylor, A. S. Sørensen, C. M. Marcus, and E. S. Polzik, “Laser cooling and optical detection of excitations in a 1 c electrical circuit,” *Physical Review Letters*, vol. 107, no. 27, p. 273601, 2011.
- [11] S. Barzanjeh, M. Abdi, G. J. Milburn, P. Tombesi, and D. Vitali, “Reversible optical-to-microwave quantum interface,” *Physical Review Letters*, vol. 109, no. 13, p. 130503, 2012.
- [12] Y.-D. Wang and A. A. Clerk, “Using interference for high fidelity quantum state transfer in optomechanics,” *Physical Review Letters*, vol. 108, no. 15, p. 153603, 2012.
- [13] L. Tian, “Adiabatic state conversion and pulse transmission in optomechanical systems,” *Physical Review Letters*, vol. 108, no. 15, p. 153604, 2012.
- [14] —, “Optoelectromechanical transducer: Reversible conversion between microwave and optical photons,” *Annalen der Physik*, vol. 527, no. 1–2, pp. 1–14, 2015.
- [15] L. Midolo, A. Schliesser, and A. Fiore, “Nano-opto-electro-mechanical systems,” *Nature Nanotechnology*, vol. 13, no. 1, pp. 11–18, 2018.
- [16] K. Liu, C. R. Ye, S. Khan, and V. J. Sorger, “Review and perspective on ultrafast wavelength-size electro-optic modulators,” *Laser & Photonics Reviews*, vol. 9, no. 2, pp. 172–194, 2015.
- [17] T. J. Kippenberg and K. J. Vahala, “Cavity optomechanics: back-action at the mesoscale,” *Science*, vol. 321, no. 5893, pp. 1172–1176, 2008.
- [18] M. Aspelmeyer, T. J. Kippenberg, and F. Marquardt, “Cavity optomechanics,” *Reviews of Modern Physics*, vol. 86, no. 4, p. 1391, 2014.
- [19] A. D. O’Connell, M. Hofheinz, M. Ansmann, R. C. Bialczak, M. Lenander, E. Lucero, M. Neeley, D. Sank, H. Wang, M. Weides, *et al.*, “Quantum ground state and single-phonon control of a mechanical resonator,” *Nature*, vol. 464, no. 7289, pp. 697–703, 2010.
- [20] J. D. Teufel, D. Li, M. Allman, K. Cicak, A. Sirois, J. Whittaker, and R. Simmonds, “Circuit cavity electromechanics in the strong-coupling regime,” *Nature*, vol. 471, no. 7337, pp. 204–208, 2011.
- [21] T. Faust, P. Krenn, S. Manus, J. P. Kotthaus, and E. M. Weig, “Microwave cavity-enhanced transduction for plug and play nanomechanics at room temperature,” *Nature Communications*, vol. 3, no. 1, pp. 1–6, 2012.
- [22] S. Gröblacher, K. Hammerer, M. R. Vanner, and M. Aspelmeyer, “Observation of strong coupling between a micromechanical resonator and an optical cavity field,” *Nature*, vol. 460, no. 7256, pp. 724–727, 2009.
- [23] E. Verhagen, S. Deléglise, S. Weis, A. Schliesser, and T. J. Kippenberg, “Quantum-coherent coupling of a mechanical oscillator to an optical cavity mode,” *Nature*, vol. 482, no. 7383, pp. 63–67, 2012.
- [24] C. Zuo, J. Van der Spiegel, and G. Piazza, “1.05-GHz CMOS oscillator based on lateral-field-excited piezoelectric AlN contour-mode MEMS resonators,” *IEEE Transactions on Ultrasonics, Ferroelectrics, and Frequency Control*, vol. 57, no. 1, pp. 82–87, 2009.
- [25] C. Zuo, C. H. Yun, P. J. Stephanou, S.-J. Park, C.-S. T. Lo, R. Mikulka, J.-H. J. Lan, M. F. Velez, R. V. Shenoy, J. Kim, *et al.*, “Cross-sectional dilation mode resonator with very high electromechanical coupling up to 10% using AlN,” in *2012 IEEE International Frequency Control Symposium Proceedings*. IEEE, 2012, pp. 1–4.
- [26] C. Zuo, C. He, W. Cheng, and Z. Wang, “Hybrid Filter Design for 5G using IPD and Acoustic Technologies,” in *2019 IEEE International Ultrasonics Symposium (IUS)*. IEEE, 2019, pp. 269–272.
- [27] K. Tonisch, V. Cimalla, C. Foerster, H. Romanus, O. Ambacher, and D. Dontsov, “Piezoelectric properties of polycrystalline AlN thin films for MEMS application,” *Sensors and Actuators A: Physical*, vol. 132, no. 2, pp. 658–663, 2006.
- [28] C. Zuo, N. Sinha, and G. Piazza, “Very high frequency channel-select MEMS filters based on self-coupled piezoelectric AlN contour-mode resonators,” *Sensors and Actuators A: Physical*, vol. 160, no. 1–2, pp. 132–140, 2010.
- [29] C. Zuo, N. Sinha, J. Van der Spiegel, and G. Piazza, “Multifrequency pierce oscillators based on piezoelectric AlN contour-mode MEMS technology,” *Journal of Microelectromechanical Systems*, vol. 19, no. 3, pp. 570–580, 2010.
- [30] A. Abramovici, W. E. Althouse, R. W. P. Drever, Y. Gursel, S. Kawamura, F. J. Raab, D. Shoemaker, L. Sievers, R. E. Spero, and K. S. Thorne, “LIGO: The Laser Interferometer Gravitational-Wave Observatory,” *Science*, vol. 256, no. 5055, pp. 325–333.
- [31] A. Freise and K. Strain, “Interferometer techniques for gravitational-wave detection,” *Living Reviews in Relativity*, vol. 13, no. 1, p. 1, 2010.
- [32] A. Arnau *et al.*, *Piezoelectric transducers and applications*. Springer, 2004, vol. 2004.
- [33] J. Rosenbaum, *Bulk acoustic wave theory and devices*. Artech House on Demand, 1988.
- [34] C. L. Zou, X. Han, L. Jiang, and H. X. Tang, “Cavity piezomechanical strong coupling and frequency conversion on an aluminum nitride chip,” *Physical Review A*, vol. 94, no. 1, p. 013812, 2016.
- [35] T. ETSI, “136 104 v16. 4.0, lte; evolved universal terrestrial radio access (e-utra); base station (bs) radio transmission and reception (3gpp ts 36.104 version 16.4.0 release 16), december 2019,” *FRANCE: ETSI (3GPP)*, pp. 36 104–20, 2019.
- [36] “Comsol multiphysics® v. 5.4,” *cn.comsol.com. COMSOL AB, Stockholm, Sweden*.
- [37] B. Auld, *Acoustic fields and waves in solids*. Wiley, 1973.
- [38] D. D. Brown and A. Freise, “Finesse,” May 2014, The software and source code is available at <http://www.gwoptics.org/finesse>. [Online]. Available: <http://www.gwoptics.org/finesse>
- [39] N. Wadefalk, R. Gawande, and S. Weinreb, “Very low noise amplifiers at 300 K for 0.7 to 1.4 GHz,” in *Proc. National Radio Science Meeting (URSI)*, 2005.
- [40] J.-B. Wang, Q.-S. Hu, J. Wang, M. Chen, and J.-Y. Wang, “Tight bounds on channel capacity for dimmable visible light communications,” *IEEE Journal of Lightwave Technology*, vol. 31, no. 23, pp. 3771–3779, 2013.
- [41] S. Kumar, H. Fan, H. Kübler, J. Sheng, and J. P. Shaffer, “Atom-based sensing of weak radio frequency electric fields using homodyne readout,” *Scientific reports*, vol. 7, p. 42981, 2017.
- [42] J. Bao, *Random Simulation Method of Classical and Quantum Dissipation System*. Beijing Science Press, 2009.